Acta Materialia 143 (2018) 291–297

Contents lists available at ScienceDirect

Acta Materialia

journal homepage: www.elsevier.com/locate/actamat

Full length article

Electron-irradiation induced defects in $Yb_2Ti_{2.05}O_7$

Ali Mostaed [a, b, *], Geetha Balakrishnan [b], Martin R. Lees [b], Richard Beanland [b]

[a] Department of Materials Science and Engineering, University of Sheffield, Sheffield S1 3JD, UK
[b] Department of Physics, University of Warwick, Gibbet Hill Road, Coventry CV4 7AL, UK

ARTICLE INFO

Article history:
Received 16 May 2017
Received in revised form
30 August 2017
Accepted 5 October 2017
Available online 12 October 2017

Keywords:
Irradiation
Pyrochlore
Dislocation
STEM
Geometric phase analysis

ABSTRACT

We present a scanning transmission electron microscopy (STEM) analysis of electron irradiation-induced defects in $Yb_2Ti_2O_7$, which form in material with a deliberate Ti excess. No defects were observed to form in stoichiometric or Yb-rich material. The defects in the Ti rich materials are regions of lower density, roughly 1.5 nm in thickness, lying along {111} or {110} planes. A minority of defects also contain extrinsic partial dislocation loops. We use geometric phase analysis of atomically-resolved annular-dark field STEM images combined with dislocation tensor analysis in a new program *BurgersVectors* to show that the Burgers vector of the partial dislocations are of $1/4\langle 110\rangle$ type. Atomically-resolved energy-dispersive X-ray analysis shows that, although some cation disorder is observed in the affected region, the material does not fully transition to a defect fluorite structure. It is proposed that these phenomena, and their absence in stoichiometric and Yb-rich material, can be explained by the presence of negatively-charged Yb vacancies that are only present in material with a Ti excess. The injection of oxygen Frenkel pairs under energetic electron irradiation provides oxygen interstitials that can neutralize positively charged Ti atoms on the Yb sites, while the mobile oxygen vacancies combine with Yb vacancies and condense to form the observed low-density regions.

1. Introduction

The behaviour of oxides when subject to energetic radiation has been an important area of materials science for some time, with applications in nuclear power generation and waste storage [1]. Pyrochlore oxides in particular have received much attention in recent years, with composition $A_2^{(3+)}B_2^{(4+)}O_7^{(2-)}$; several hundred pyrochlores are known, with combinations of different *A* and *B* cations [2]. Recent radiation damage studies in these materials have focused on their response to swift heavy ions with energies in the MeV to GeV range [3–15]. Such high-energy ions deposit a significant amount of energy into the crystal lattice, leaving behind a track with an amorphous core surrounded by altered material [6,12,14,16,17]. Some pyrochlores show remarkable resistance to amorphization [3]. Here, we observe and characterize defects formed in the pyrochlore oxide $Yb_2Ti_2O_7$ in a rather different energy regime, namely under irradiation by 200 keV electrons. The defects take the form of planar faults and faulted dislocation loops a few nm in diameter, and only form in material with a deliberate Ti excess. By using geometric phase analysis (GPA) to extract the dislocation tensor content of atomic resolution scanning transmission electron microscopy (scanning TEM, or STEM) images, we find that dislocation loops have Burgers vectors $1/4\langle 110\rangle$. Our aims are to clarify the effect of low energy irradiation (which is present in any radiation cascade and plays an important role e.g. in the nuclear fuel/waste environment), as well as undertaking a study of the fundamental processes in selective displacement of the oxygen sublattice in pyrochlore oxides.

As noted by Bohr, when an energetic charged particle, e.g. ion or electron, penetrates a solid it interacts with the nuclei as well as the electrons of the material [18]. This gives rise to two different mechanisms; electronic stopping (energy loss to the target's electrons) and nuclear stopping (energy loss to the target's positive atomic cores) [18–20]. Nuclear stopping is dominant for relatively slow ions, ($E \leq 100$ keV/amu) and is a consequence of ballistic collisions between the ion and the nuclei of atoms in the target. Consequently, the ion's kinetic energy is partly transmitted to an atom in the target material, either displacing the atom from its site or transferred to the material as a whole. For higher energy ions electronic stopping is dominant, i.e. inelastic collisions between the moving ion and electrons, which can be bound or free, in the target [18].

* Corresponding author. Department of Materials Science and Engineering, University of Sheffield, Sheffield S1 3JD, UK.
E-mail address: a.mostaed@sheffield.ac.uk (A. Mostaed).

https://doi.org/10.1016/j.actamat.2017.10.028
1359-6454/

In the case of electron irradiation, electronic stopping dominates. The energy transfer is too small to displace atoms from their sites, although material changes can be induced through breaking of bonds. Nuclear stopping also occurs, but only a small fraction of the kinetic energy is transferred to the target nucleus of target because of momentum conservation [18,20]. The maximum transferred energy (T_m) with an elastic collision between the projectile and target atom can be roughly calculated by: [21]

$$T_m = \frac{2E}{Mc^2}\left(E + 2m_0c^2\right) \quad (1)$$

where m_0, M and E are the electron mass (at rest), target atom mass and initial kinetic energy of the electron [21]. Applying Eq. (1) to $Yb_2Ti_2O_7$, a 200 keV electron can transfer ~33 eV to an oxygen atom, i.e. enough kinetic energy to produce an oxygen Frenkel pair. However, energy transfer is insufficient to displace a fully bound Yb atom (~3 eV) or a Ti atom (~11 eV). We note that one would expect such energies in the tail of any displacement cascade and we therefore expect this work to also have relevance for applications involving higher-energy radiation.

The condensation of point defects into planar defects (e.g. Frank loops) in response to irradiation is well documented in e.g. metals [22–25], semiconductors [26–28] and several types of oxides (e.g. perovskite, stabilized zirconia and fluorite) [29–33]. Surprisingly, there appear to be no studies of such defects in pyrochlores [34] and even basic characterisation of dislocations in these materials lacks any detail [30]. We therefore turn to studies of the closely-related fluorite structure for an indication of which defects may form. Fluorite, like pyrochlore, is a mixture of metal cations and oxygen anions, although fluorite has the general formula $R^{(4+)}O_2^{(2-)}$ where R is a metal cation such as U, Ce, Zr, etc. Dislocations in such ionic materials, where charge balance is important, can in principle have high electrostatic charges associated with unsatisfied bonding in the dislocation core [35]. Any such charges are usually considered to be balanced by an atmosphere of point defects of opposite sign, or reconstruction of the core itself to provide equal and opposite charge along the dislocation line [36,37]. Crystals with the fluorite structure have a face-centred cubic (fcc) lattice (Fig. 1) with typical lattice parameter ~0.54 nm. Perfect dislocations have been observed with Burgers vectors equal to the shortest lattice translation vector, $\boldsymbol{b} = 1/2\langle 110\rangle$, (typical of fcc materials since they have the smallest self-energy, proportional to b^2) and are expected to have reconstructed (charge-balanced) cores [35]. Dissociation of a $\boldsymbol{b} = 1/2\langle 110\rangle$ dislocation into two $\boldsymbol{b} = 1/6\langle 112\rangle$ Shockley partials does not occur due to the high electrostatic charge this would entail [36]. In radiation damage studies of fluorites such as UO_2, formation of $\boldsymbol{b} = 1/3\langle 111\rangle$ Frank loops through condensation of interstitials to form a complete O-R-O $\{111\}$ layer has been observed [38]. In CeO_2, oxygen interstitials have been found to condense into $\boldsymbol{b} = 1/9\langle 111\rangle$ Frank loops at low irradiation energies, while both Ce and O interstitials can produce perfect $\boldsymbol{b} = 1/2\langle 110\rangle$ Frank loops at higher energies [21].

Pyrochlore can be considered an ordered superstructure of the fluorite structure, as is apparent from Fig. 1, which shows an octant of the pyrochlore cell and its similarity with the fluorite structure [15]. Although the pyrochlore lattice is still face-centred cubic, the A and B cations are ordered into Kagome patterns on the $\{111\}$ planes and an oxygen atom is missing in comparison with the fluorite structure. This oxygen vacancy produces displacements of the remaining oxygen atoms and a lack of equivalence between them, with Wyckoff 48f-site and 8a-site oxygen atoms in each complete pyrochlore unit cell (Fig. 1). Previous studies have shown that radiation damage in pyrochlores can produce a 'defect fluorite' structure [8], with the stoichiometry of pyrochlore but mixing of the cation sublattice and oxygen vacancies to produce a structure that has an 'average' symmetry equivalent to that of fluorite. Indeed, it has been proposed that the ability of different pyrochlores to withstand swift ion irradiation is correlated with their propensity to form defect fluorite structures [9,15,39].

The fcc unit cell of the nominal pyrochlore structure is doubled in all directions in comparison with the fluorite structure, giving a lattice parameter ~1.1 nm. The paucity of observations of dislocations in pyrochlores is perhaps due to the large Burgers vector of a superdislocation $\boldsymbol{b} = 1/2\langle 110\rangle$ (~0.75 nm), and the large self-energy that results. The equivalent to a $\boldsymbol{b} = 1/2\langle 110\rangle$ fluorite dislocation is an imperfect $\boldsymbol{b} = 1/4\langle 110\rangle$ partial dislocation in pyrochlore, which bounds an $\boldsymbol{R} = 1/4[110]$ anti-phase boundary (APB). One may therefore expect a superdislocation $\boldsymbol{b} = 1/2\langle 110\rangle$ to dissociate into a pair of $\boldsymbol{b} = 1/4\langle 110\rangle$ partials and an APB. It also seems reasonable that radiation damage in pyrochlores may produce faulted interstitial Frank loops analogous to those previously observed in fluorites – i.e. with fault vectors $\boldsymbol{b} = 1/18\langle 111\rangle$,

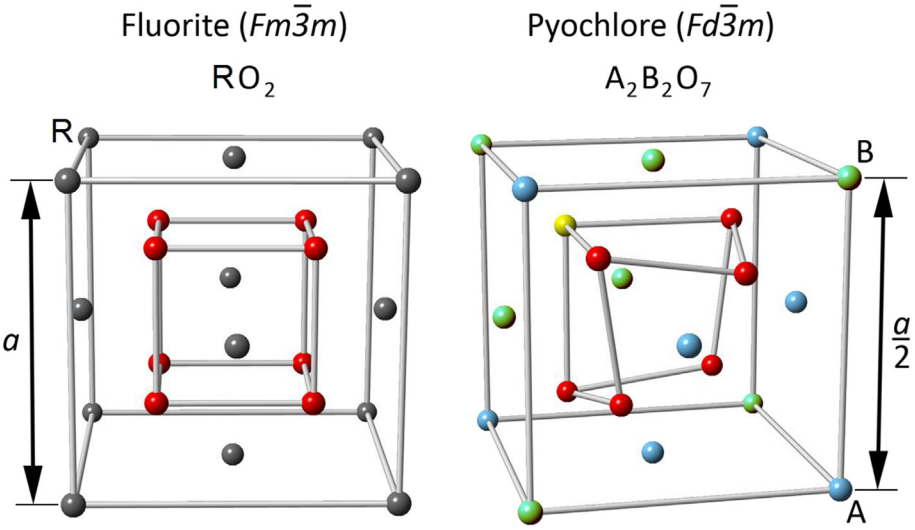

Fig. 1. Left: Face-centred cubic fluorite structure, with R metal cations grey and oxygen anions red. Right: one octant of the pyrochlore structure, with A cations green, B cations blue, 48f oxygen anions red and 8b oxygen anions yellow. (For interpretation of the references to colour in this figure legend, the reader is referred to the web version of this article.)

1/6⟨111⟩ or 1/4⟨110⟩.

Using TEM at an accelerating voltage of 200 kV, we have examined $Yb_2Ti_2O_7$ with nominal stoichiometry as well as material with excess Yb or Ti of a few atomic percent. Notably, we observe the formation of extended defects under electron irradiation only in Ti-rich material and we report only on Ti-rich material in this work.

2. Methods

Polycrystalline (powder) samples of $Yb_2Ti_{2.05}O_7$ with 2.5 at.% excess Ti were synthesized using a solid state reaction method. Appropriate quantities of Yb_2O_3 and TiO_2 powders were repeatedly ground, pressed into pellets, and sintered at 1150 °C for 12 h, with a final firing at 1350 °C for 24 h. Specimens were prepared for transmission electron microscopy using standard routes, i.e. mechanical grinding and polishing followed by ion milling to electron transparency. A final low-energy ion mill of 500 eV was used to remove surface damage. Data were obtained with a doubly-corrected JEOL ARM200F microscope at 200 kV. In order to obtain data with a good signal to noise ratio, unaffected by specimen drift, up to sixty images were collected sequentially, all with a short time of 10 μs/pixel. The images were aligned using normalized cross-correlation and summed to produce high quality, low noise data. Annular dark field (ADF) images were collected with an ADF detector inner angle of ~4.6α, where α is the half-convergence angle of the electron probe (15 mrad). Data were normalized to the incident beam intensity using calibrated brightness/contrast levels, a map of the ADF detector response and an image of the diffraction pattern falling on the detector, following an approach similar to that of LeBeau and co-workers [40]. Atomic resolution energy-dispersive x-ray (EDX) spectroscopy measurements were obtained with a windowless Oxford Instruments X-max 100 silicon drift x-ray detector.

3. Results

Defects were observed to form in TEM mode with an electron beam with current ~2.5 μA focused to an electron probe a few tens of nm in size, giving roughly 10^6 A/cm^2 at the sample. They appeared to form instantaneously, and were subsequently stable and unchanging with lower beam fluences. Fig. 2 shows ADF-STEM images of the irradiation-induced defects. They appear in this image, taken with the incident beam direction along [1$\bar{1}$0], as dark lines parallel to {111} planes. We also observed occasional defects as dark lines parallel to {011} planes (not shown). Since contrast in ADF images is primarily proportional to mass-thickness, this indicates material that is either of much lower density, or is thinner, than the matrix. A faint 'halo' of brighter material is visible around the defects, which may indicate denser material or changes in the secondary contrast mechanism of electron channelling (static atomic displacements have been shown to result in an increased ADF signal, e.g. Ref. [41]).

Two types of defect were observed; the majority induced no measurable strain in the crystal, while a minority had long-range strain fields and dislocation character. The two types of defect appear identical and cannot be distinguished in Fig. 2(a). A higher magnification ADF-STEM image of the majority type is shown in Fig. 2(b). The atomic columns of the crystal are clearly resolved in this image, of which there are three types (see inset): *i*) Yb columns, which appear brightest due to the high atomic number of Yb; *ii*) Ti columns, which are faint; and *iii*) mixed columns (50% Ti + 50% Yb), with intermediate contrast, denoted *M*. Oxygen atoms are not visible in ADF images, although careful analysis can show their influence [42]. In Fig. 2(b) it is clear that the defect has a width of 4–6 atomic {111} planes (~1.5 nm) with patchy dark contrast, and is in fact only roughly aligned along {111}. The change in contrast in a similar, larger defect is shown in Fig. 2(c). EDX data (Fig. 2(d)) show that both Ti and Yb signals have lower intensities in the defect area. In addition, the change in contrast in a defect aligned along {011} is analyzed for each atom column in Fig. 3. This defect has a thickness of about eight {011} atomic planes, or ~1.5 nm (yellow dashed lines in Fig. 3(a)). Fig. 3(b) shows a histogram of the mean integrated intensities from Voronoi cells, centred on each atomic column in Fig. 3(a). This reveals that the contrast of the Ti*, Yb* and M^* atom columns in the defect are all less intense by approximately the same degree (~7%) than the analogous Ti, Yb and *M* atom columns outside. The relative intensities of the Yb and Ti atom columns are unchanged in both the ADF and EDX data, showing that there has been no transition to a disordered 'defect fluorite' structure. This indicates that these defects may simply be voids, or trenches on the specimen surface. Interestingly, the material surrounding the defect displayed in Fig. 3(a) shows clear evidence of site-swapping between the cation sublattices as shown in Fig. 3(c). Occasional Ti sites have significantly brighter contrast than their neighbours, indicating the 'stuffing' of Yb on Ti sites, Yb'_{Ti}.

An example of the second (minority) type of defect with a long-range strain field is shown in Fig. 4. Fig. 4(a) shows that this defect is also 4–6 {111} planes (~1.5 nm) in thickness, but in this case an APB is visible with Yb-rich (bright) planes above the defect aligned with Ti-rich (faint) planes below. Fourier filtered images of Fig. 4(a), obtained using the ±2$\bar{2}$2 or ±222 spots in the FFT (inset, Fig. 4(a))

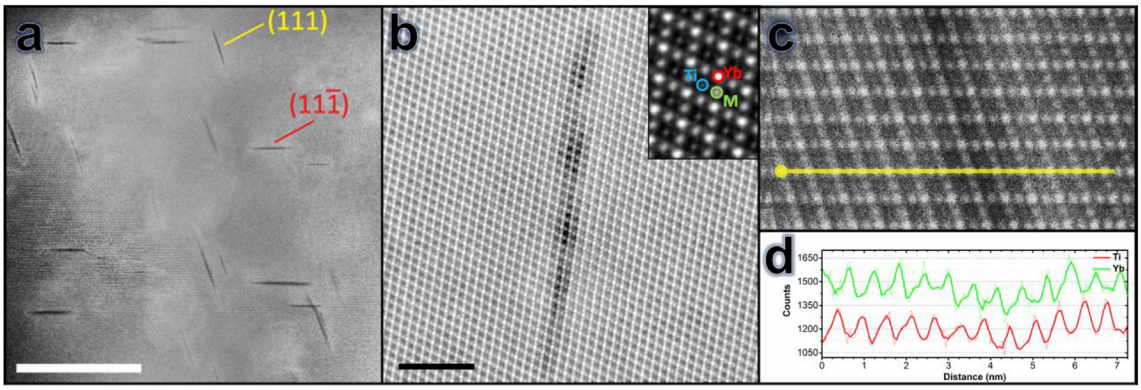

Fig. 2. (a) ADF-STEM image of planar defects in $Yb_2Ti_{2.05}O_7$ irradiated with 200 keV electrons. The incident beam direction is along [1$\bar{1}$0] and the scale bar is 100 nm. (b) One of the dislocation-free defects at higher magnification, scale bar is 5 nm. (c) ADF-STEM image taken from a large strain-free defect. (d) The EDX line scan across the defect shown in (c).

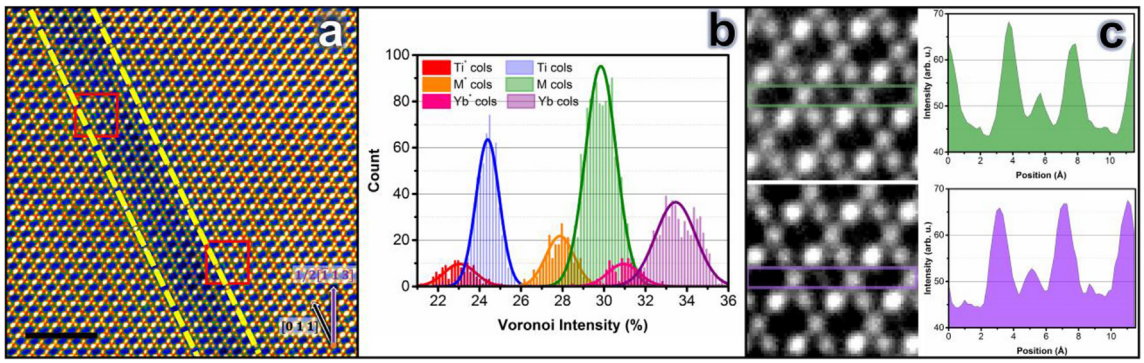

Fig. 3. (a) ADF-STEM image of a strain-free defects viewed along [411] (scale bar is 2 nm), (b) histogram of the extracted mean integrated intensities from the ADF image shown in (a), using Voronoi cells centred on each atomic column and (c) anomalously bright Ti columns present in the areas marked by red squares in (a). (For interpretation of the references to colour in this figure legend, the reader is referred to the web version of this article.)

are shown in Fig. 4(b) and (c) respectively. These images reveal that two dislocation dipoles are associated with the defect, visible as extra 222 and $\overline{2}\overline{2}2$ half-planes, $\delta1$–$\delta4$. Interestingly, the defect is larger than the dislocation loops and extends some distance to the left, where it has a similar structure to the majority defects. Strain fields, obtained by geometric phase analysis (GPA) using the program Strain++ [43,44] are shown in Fig. 4(d–f). Here, ε_{xx} and ε_{yy} show the $[\overline{1}\overline{1}2]$ and [111] components, respectively, and ε_{xy} shows the shear strains. This shows that the dislocations on the left do not coincide with the position of the defect; $\delta3$ lies above, and $\delta4$ lies below, the affected region. Fig. 4(d–f) also show that there is no significant strain associated with the darker areas of the defect, either inside the dislocation loops or outside them, to the left of Fig. 4.

To characterize these dislocation loops, it is necessary to know their Burgers vector. Two issues arise. First, since TEM images are a projection of the crystal onto the image plane, Burgers vector components parallel to the beam cannot be measured and must be inferred through other means. Only the projected Burgers vector, $\boldsymbol{b}'$, is measured, rather than the actual Burgers vector $\boldsymbol{b}$. Second, an accurate measure of the projected Burgers vector of partial dislocations from atomic resolution ADF-STEM images of a complex crystal structure is not straightforward. The atomic displacements are some fraction of an interatomic spacing and therefore difficult to perform by inspection of the image – e.g. the defects $\delta3$ and $\delta4$ are difficult to locate in Fig. 4(a) by eye and are certainly not amenable to Burgers circuit analysis. We have therefore developed the approach of Kioseoglou et al. [45] into a program *BurgersVectors* [46] to analyze our images of these defects. This approach extracts the two-dimensional components of Nye's dislocation density tensor, a_x and a_y, from the 2D deformation fields obtained by applying GPA to the images. The result is a peak, with amplitude corresponding to the projected Burgers vector component (following the finish-start/right hand FS/RH convention with the dislocation line direction into the image), centred at the position of the dislocation core, giving unambiguous information on the

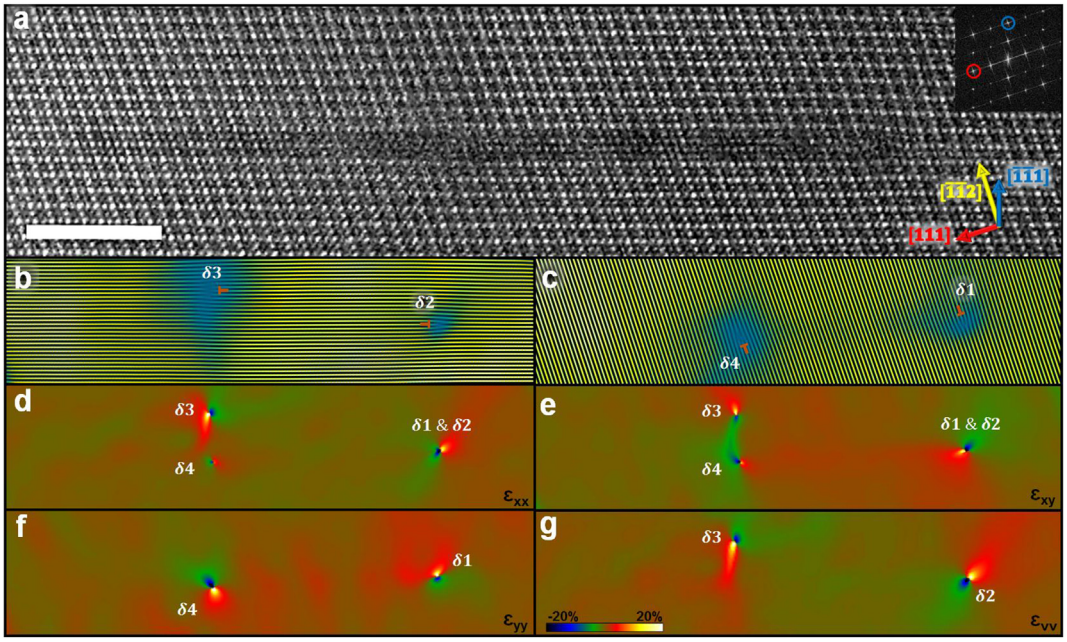

Fig. 4. (a) $[1\overline{1}0]$ ADF-STEM image from a faulted defect (scale bar is 5 nm). (b) and (c) Fourier filtered images obtained by choosing $\pm\overline{2}\overline{2}2$ (FFT inset, blue) and ±222 spots (FFT inset, red), respectively. GPA strain components (d) ε_{xx} (e) ε_{xy} and (f) ε_{yy}; where $\boldsymbol{x} = [\overline{1}\overline{1}2]$ and $\boldsymbol{y} = [111]$. (g) strain component ε_{vv} where $\boldsymbol{v} = [\overline{1}11]$. (For interpretation of the references to colour in this figure legend, the reader is referred to the web version of this article.)

magnitude and location of a defect even when the shift of lattice fringes is only fractional. The dislocations in Fig. 4 are analyzed using this software in Fig. 5. The defect at the right hand edge of the defect is shown in Fig. 5(a), with its dislocation density tensor components in Fig. 5(b) and (c). The dislocations $\delta 1$ and $\delta 2$ appear in slightly different places in Fig. 5(b), although they are essentially coincident when plotted on the image (orange and white dots, Fig. 5(a)). A similar analysis of dislocations $\delta 3$ and $\delta 4$ is shown in Fig. 5(d) and (e). The projected Burgers vectors are determined to be $\boldsymbol{b}'_{\delta 1} = 1/8[\bar{1}\bar{1}2]$, $\boldsymbol{b}'_{\delta 2} = 1/8[\bar{1}\bar{1}2]$, and $\boldsymbol{b}'_{\delta 2} = 1/8[11\bar{2}] = -\boldsymbol{b}'_{\delta 2}$, $\boldsymbol{b}'_{\delta 4} = 1/8[112] = -\boldsymbol{b}'_{\delta 1}$. This is consistent with their appearance as dislocation dipoles in Fig. 4(b) and (c) as well as the observation that dislocation $\delta 3$ is invisible in the ε_{yy} image, indicating that its projected Burgers vector is parallel to $\boldsymbol{x} = [\bar{1}\bar{1}2]$. Similarly, the dislocation $\delta 4$ is invisible in the ε_{vv} GPA strain map (Fig. 4(g)), where $\boldsymbol{v} = [\bar{1}\bar{1}1]$, indicating that it has a projected Burgers vector parallel to $[\bar{1}12]$.

Burgers vectors of $1/8\langle 112\rangle$ are not feasible for the pyrochlore structure and we therefore consider the Burgers vector components $\boldsymbol{b}_z$ along the electron beam that would produce physically reasonable defects. The identical location of dislocations $\delta 1$ and $\delta 2$ (to within one metal atom spacing) implies that they have combined to form a single dislocation, which would require the Burgers vectors to be such that a dislocation reaction is energetically favourable, i.e. $\boldsymbol{b}^2_{\delta 1+\delta 2} \leq \boldsymbol{b}^2_{\delta 1} + \boldsymbol{b}^2_{\delta 2}$. There are two possibilities that are consistent with this constraint. *i*) The components $\boldsymbol{b}_z$ are equal and opposite for $\delta 1$ and $\delta 2$, i.e. $\boldsymbol{b}_{\delta 1} = 1/4[0\bar{1}\bar{1}]$ and $\boldsymbol{b}_{\delta 2} = 1/4[\bar{1}01]$, (or equally likely, $\boldsymbol{b}_{\delta 1} = 1/4[\bar{1}0\bar{1}]$ and $\boldsymbol{b}_{\delta 2} = 1/4[0\bar{1}1]$). In this case $\boldsymbol{b}_{\delta 1+\delta 2} = 1/4[\bar{1}\bar{1}0]$, which is also the result of the Burgers circuit analysis in Fig. 5(a). *ii*) The components $\boldsymbol{b}_z$ are the same for $\delta 1$ and $\delta 2$, i.e. $\boldsymbol{b}_{\delta 1} = 1/4[0\bar{1}\bar{1}]$ and $\boldsymbol{b}_{\delta 2} = 1/4[0\bar{1}1]$, (or equally likely, $\boldsymbol{b}_{\delta 1} = 1/4[\bar{1}01]$ and $\boldsymbol{b}_{\delta 2} = 1/4[\bar{1}01]$). In this case $\boldsymbol{b}_{\delta 1+\delta 2} = 1/2[0\bar{1}0]$ or $1/2[\bar{1}00]$. It is not possible to distinguish further between these possibilities without additional information, but it is clear that the defect is extrinsic dislocation loop having both Frank and Shockley character formed by dislocations with Burgers vectors of the type $1/4\langle 110\rangle$.

As shown in Fig. 5(a), the stacking sequence *ABCABC* … of the $\{\bar{1}\bar{1}1\}$ planes is *ABC**B**ABC* in the defect region as a consequence of introduction of an extra $(\bar{2}\bar{2}2)$ half-plane (marked with a white *B*). According to the atomic resolution EDX elemental maps data shown in Fig. 6, the extra $(\bar{2}\bar{2}2)$ plane contains both Yb and Ti atoms, i.e. the defect does not appear to be due to the condensation of an excess of one particular type of atom (e.g. interstitial Ti). Furthermore, both the Yb-rich and Ti-rich $\{111\}$ planes (Fig. 6(c) and (d)) are more or less intact up to the anti-phase boundary induced. However, significant cation disorder is visible at the defect with both Yb and Ti site swapping clearly visible, indicating that the material has changed towards a defect fluorite structure even though the cation sublattices are not completely mixed.

4. Discussion

Defects only form under electron irradiation in material with excess Ti, and this behaviour is presumably related to differences in material structure and stability caused by the deviation from exact stoichiometry. Excess $Ti^{(4+)}$ can be accommodated in the pyrochlore structure by substitution on $Yb^{(3+)}$ sites and this is much more favourable than interstitial Ti (Substitution of *A*-cations on *B* sites, A'_B, is commonly known as 'stuffing' [47]; here we have the opposite effect, 'anti-stuffing', $B^{\bullet}_A$). In order to maintain overall charge neutrality in the material the surplus $(1+)$ positive charge produced by each anti-stuffing substitution $Ti^{\bullet}_{Yb}$ must be compensated or balanced by some mechanism. For example, since Ti can exist in a range of charge states it may simply change from $Ti^{(4+)}$ to $Ti^{(3+)}$ when on the Yb site [42,48]. Alternatively, net charge balance may be obtained by the presence of other, negatively charged, point defects. Stanek et al. [49] have calculated energies of point defects in pyrochlores, although they did not consider any changes in charge state. For $Yb_2Ti_2O_7$ they found that, in the presence of $Ti^{\bullet}_{Yb}$, the negatively-charged point defect $(3-)$ Yb vacancy, V'''_{Yb} had significantly lower energy than the oxygen interstitial O''_i and gave the following equation for charge-balanced excess Ti (in Kröger-Vink notation [50]):

$$7(TiO_2) + 4Yb^{\times}_{Yb} \longrightarrow 3Ti^{\bullet}_{Yb} + V'''_{Yb} + 2(Yb_2Ti_2O_7). \quad (2)$$

In our Ti-rich material therefore, Eq. (2) predicts no change in oxygen stoichiometry and the formula $(Yb_{1.95}Ti_{0.05})Ti_2O_7$. Nevertheless, since Stanek et al. [49] did not consider changes in charge state of Ti or any other ion there remains some uncertainty about

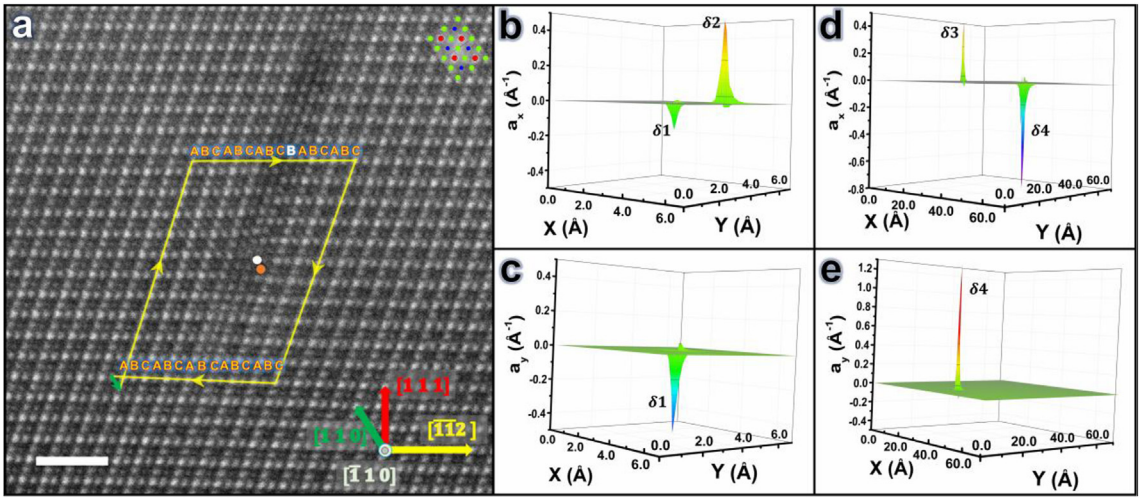

Fig. 5. (a) ADF-STEM image of the right hand end of the faulted defect shown in Fig. 4 with overlaid Burgers circuit. The position of $\delta 1$ and $\delta 2$ are marked by the white and orange solid-circles, respectively (scale bar is 2 nm). The image is rotated 108° clockwise with respect to Fig. 4. (b) and (c) Outputs from the program *BurgersVectors* applied to Fig. 5(a), showing the *x*- and *y*- components of the dislocation density tensor (a_x and a_y) respectively. (d) and (e) Similar output for dislocations $\delta 3$ and $\delta 4$. (For interpretation of the references to colour in this figure legend, the reader is referred to the web version of this article.)

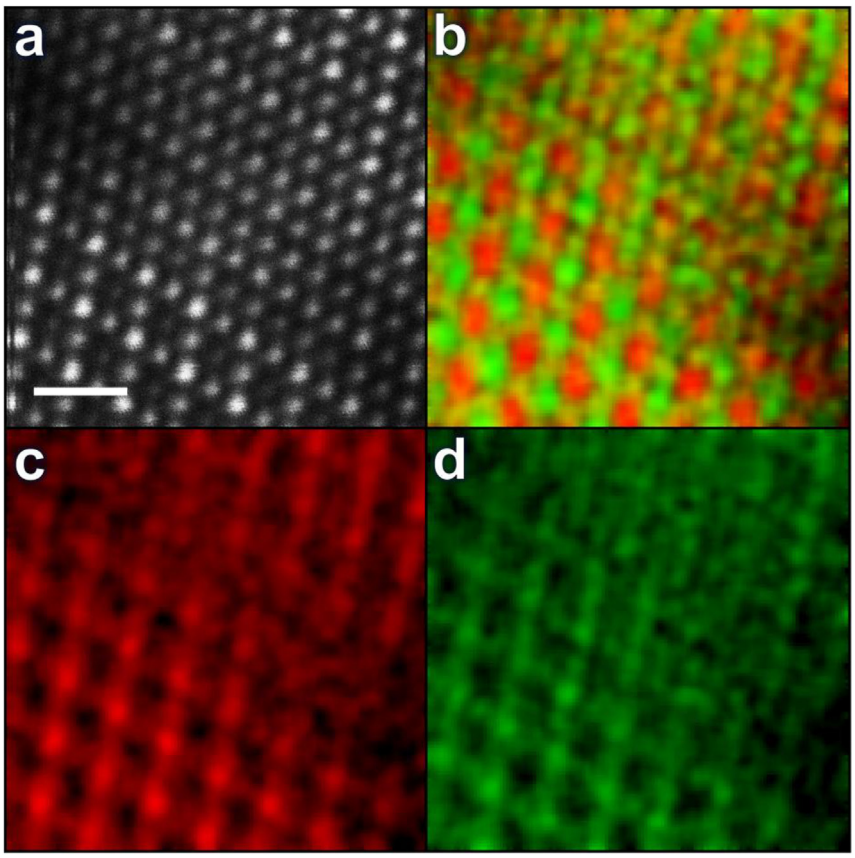

Fig. 6. (a) ADF-STEM image across the defect shown in Fig. 4(a) (scale bar is 0.5 nm). (b) Atomic scale EDX map from (a); Ti and Yb signals shown in red and green, respectively. (c) Ti and (d) Yb EDX elemental maps from (a). (For interpretation of the references to colour in this figure legend, the reader is referred to the web version of this article.)

the actual charge balance mechanism. Excess Yb, on the other hand, is expected to substitute on the Ti site Yb'_{Ti} and produce (2+) oxygen vacancies $V_O^{\bullet\bullet}$, i.e. [49]

$$2(Yb_2O_3) + 2Yb_{Yb}^{\times} + O_O^{\times} \longrightarrow 2Yb'_{Ti} + V_O^{\bullet\bullet} + Yb_2Ti_2O_7, \quad (3)$$

giving $Yb_2(Ti_{2-x}Yb_x)O_{7-x/2}$. Stoichiometric $Yb_2Ti_2O_7$ may of course be expected to have small populations of point defects at equilibrium.

As mentioned in the introduction, the energy transferred during irradiation by 200 keV electrons is sufficient to produce oxygen Frenkel pairs [21], i.e.

$$O_O^{\times} \longrightarrow O_i'' + V_O^{\bullet\bullet}, \quad (4)$$

but is not enough to displace fully bound Yb or Ti from their lattice sites. The injection of oxygen interstitials O_i'' due to electron irradiation provides an alternative mechanism to neutralize $Ti_{Yb}^{\bullet}$ [49]

$$8(TiO_2) + 4Yb_{Yb}^{\times} \longrightarrow 4Ti_{Yb}^{\bullet} + 2O_i'' + 2(Yb_2Ti_2O_7) \quad (5)$$

giving $(Yb_{1.95}Ti_{0.05})Ti_2O_{7-\xi}$, where ξ indicates the presence of the oxygen vacancies. Additionally, the positively charged oxygen vacancies $V_O^{\bullet\bullet}$ and negatively charged Yb vacancies V_{Yb}''' will attract each other. The observed behaviour may thus be the result of the higher mobility of vacancies in comparison with interstitials; rather than the material recovering through the reverse reaction of Eq. (4), the vacancies agglomerate to produce regions of lower density. We note that this mechanism is not expected to operate in Yb-rich material since Yb excess is already balanced by $V_O^{\bullet\bullet}$ (Eq. (3)) and in this case there are no negatively charged vacancies available to form vacancy agglomerations. Interestingly, the defect loops observed are interstitial defects, i.e. there is an *additional* plane of cations marked by the extra '*B*' in Fig. 5(a), even though the surrounding material contains a high density of cation vacancies. This behaviour is also consistent with the proposal that the agglomerations are controlled by the presence of oxygen vacancies.

5. Conclusions

In summary, we have observed electron irradiation-induced defects in $Yb_2Ti_2O_7$ with a deliberate Ti excess of 2.5 at.% using transmission electron microscopy. The defects are regions of lower density, roughly 1.5 nm in thickness, arranged along {111} or {110} planes. Some defects contain extrinsic dislocation loops bounded by dislocations with Burgers vectors of $1/4\langle 110\rangle$. Atomically-resolved EDX shows that, although some cation disorder is observed in the affected region, the material does not fully transition to a defect fluorite structure. It is proposed that these phenomena, and their absence in stoichiometric and Yb-rich material, can be explained by the presence of negatively-charged Yb vacancies in the as-produced material. The injection of oxygen Frenkel pairs under energetic electron irradiation provides both an alternative means to neutralize positively charged Ti atoms on Yb sites and mobile positively-charged oxygen vacancies, which combine with Yb vacancies and condense to form the observed low-density regions.

Acknowledgements

Part of the work was supported by EPSRC, UK, Grants M028771/1 and EP/M028771/1. A.M. acknowledges the University of Warwick Chancellor's International Scholarship for financial support. Raw data and the program *BurgersVectors* may be obtained from http://wrap.warwick.ac.uk/88297.

References

[1] D. Simeone, J.M. Costantini, L. Luneville, L. Desgranges, P. Trocellier, P. Garcia, Characterization of radiation damage in ceramics: old challenge new issues? J. Mater. Res. 30 (9) (2015) 1495–1515.
[2] M.A. Subramanian, G. Aravamudan, G.V.S. Rao, Oxide Pyrochlores - a review, Prog. Solid State Chem. 15 (2) (1983) 55–143.
[3] M. Lang, F. Zhang, J. Zhang, J. Wang, J. Lian, W.J. Weber, B. Schuster, C. Trautmann, R. Neumann, R.C. Ewing, Review of $A_2B_2O_7$ pyrochlore response to irradiation and pressure, Nucl. Instrum. Methods Phys. Res. Sect. B: Beam Interact. Mater. Atoms 268 (19) (2010) 2951–2959.
[4] J. Shamblin, C.L. Tracy, R.C. Ewing, F. Zhang, W. Li, C. Trautmann, M. Lang, Structural response of titanate pyrochlores to swift heavy ion irradiation, Acta Mater. 117 (2016) 207–215.
[5] T.C. Kaspar, J.G. Gigax, L. Shao, M.E. Bowden, T. Varga, V. Shutthanandan, S.R. Spurgeon, P. Yan, C. Wang, P. Ramuhalli, C.H. Henager Jr., Damage evolution of ion irradiated defected-fluorite $La_2Zr_2O_7$ epitaxial thin films, Acta Mater. 130 (2017) 111–120.
[6] M. Lang, J. Lian, J. Zhang, F. Zhang, W.J. Weber, C. Trautmann, R.C. Ewing, Single-ion tracks in $Gd_2Zr_{2-x}Ti_xO_7$ pyrochlores irradiated with swift heavy ions, Phys. Rev. B 79 (22) (2009) 224105.
[7] M. Lang, J. Lian, J.M. Zhang, F.X. Zhang, W.J. Weber, C. Trautmann, R.C. Ewing, Single-ion tracks in $Gd_2Zr_{2-x}Ti_xO_7$ pyrochlores irradiated with swift heavy ions, Phys. Rev. B 79 (22) (2009) 224105.
[8] R. Sachan, Y. Zhang, X. Ou, C. Trautmann, M.F. Chisholm, W.J. Weber, New insights on ion track morphology in pyrochlores by aberration corrected scanning transmission electron microscopy, J. Mater. Res. 32 (5) (2017) 928–935.
[9] K.E. Sickafus, R.W. Grimes, J.A. Valdez, A. Cleave, M. Tang, M. Ishimaru, S.M. Corish, C.R. Stanek, B.P. Uberuaga, Radiation-induced amorphization resistance and radiation tolerance in structurally related oxides, Nat. Mater. 6 (3) (2007) 217–223.
[10] A. Soulié, D. Menut, J.-P. Crocombette, A. Chartier, N. Sellami, G. Sattonnay, I. Monnet, J.-L. Béchade, X-ray diffraction study of the $Y_2Ti_2O_7$ pyrochlore disordering sequence under irradiation, J. Nucl. Mater. 480 (2016) 314–322.
[11] B.P. Uberuaga, M. Tang, C. Jiang, J.A. Valdez, R. Smith, Y. Wang, K.E. Sickafus, Opposite correlations between cation disordering and amorphization resistance in spinels versus pyrochlores, Nat. Commun. 6 (2015) 8750.
[12] S.X. Wang, L.M. Wang, R.C. Ewing, K.V. Govindan Kutty, Ion irradiation of rare-earth- and yttrium-titanate-pyrochlores, Nucl. Instrum. Methods Phys. Res. Sect. B: Beam Interact. Mater. Atoms 169 (1–4) (2000) 135–140.
[13] S.X. Wang, L.M. Wang, R.C. Ewing, K.V.G. Kutty, Ion irradiation effects for two pyrochlore compositions: $Gd_2Ti_2O_7$ and $Gd_2Zr_2O_7$, in: S.J. Zinkle, G.E. Lucas, R.C. Ewing, J.S. Williams (Eds.), Microstructural Processes in Irradiated Materials, 1999, pp. 355–360.
[14] Y. Zhang, J. Jagielski, I.-T. Bae, X. Xiang, L. Thomé, G. Balakrishnan, D.M. Paul, W.J. Weber, Damage evolution in Au-implanted $Ho_2Ti_2O_7$ titanate pyrochlore, Nucl. Instrum. Methods Phys. Res. Sect. B: Beam Interact. Mater. Atoms 268 (19) (2010) 3009–3013.
[15] K.E. Sickafus, L. Minervini, R.W. Grimes, J.A. Valdez, M. Ishimaru, F. Li, K.J. McClellan, T. Hartmann, Radiation tolerance of complex oxides, Science 289 (5480) (2000) 748–751.
[16] J. Lian, L. Wang, J. Chen, K. Sun, R.C. Ewing, J.M. Farmer, L.A. Boatner, The order-disorder transition in ion-irradiated pyrochlore, Acta Mater. 51 (5) (2003) 1493–1502.
[17] S. Moll, G. Sattonnay, L. Thomé, J. Jagielski, C. Decorse, P. Simon, I. Monnet, W.J. Weber, Irradiation damage in $Gd_2Ti_2O_7$ single crystals: ballistic versus ionization processes, Phys. Rev. B 84 (6) (2011) 064115.
[18] A.V. Krasheninnikov, K. Nordlund, Ion and electron irradiation-induced effects in nanostructured materials, J. Appl. Phys. 107 (7) (2010) 071301.
[19] M.S. Dresselhaus, R. Kalish, Ion Implantation in Diamond, Graphite, and Related Materials, Springer-Verlag, 1992.
[20] J.F. Ziegler, Stopping of energetic light ions in elemental matter, J. Appl. Phys. 85 (3) (1999) 1249–1272.
[21] K. Yasunaga, K. Yasuda, S. Matsumura, T. Sonoda, Electron energy-dependent formation of dislocation loops in CeO_2, Nucl. Instrum. Methods Phys. Res. Sect. B: Beam Interact. Mater. Atoms 266 (12–13) (2008) 2877–2881.
[22] Y. Dai, X. Jia, J.C. Chen, W.F. Sommer, M. Victoria, G.S. Bauer, Microstructure of both as-irradiated and deformed 304L stainless steel irradiated with 800 MeV protons, J. Nucl. Mater. 296 (2001) 174–182.
[23] E.H. Lee, M.H. Yoo, T.S. Byun, J.D. Hunn, K. Farrell, L.K. Mansur, On the origin of deformation microstructures in austenitic stainless steel: Part II - Mechanisms, Acta Mater. 49 (16) (2001) 3277–3287.
[24] Y.N. Osetsky, A. Serra, B.N. Singh, S.I. Golubov, Structure and properties of clusters of self-interstitial atoms in fcc copper and bcc iron, Philos. Mag. a-Phys. Condens. Matter Struct. Defects Mech. Prop. 80 (9) (2000) 2131–2157.
[25] C. Pokor, Y. Brechet, P. Dubuisson, J.P. Massoud, A. Barbu, Irradiation damage in 304 and 316 stainless steels: experimental investigation and modeling. Part I: evolution of the microstructure, J. Nucl. Mater. 326 (1) (2004) 19–29.
[26] G.Z. Pan, K.N. Tu, A. Prussin, Size-distribution and annealing behavior of end-of-range dislocation loops in silicon-implanted silicon, J. Appl. Phys. 81 (1) (1997) 78–84.
[27] K.S. Jones, E.L. Allen, H.G. Robinson, D.A. Stevenson, M.D. Deal, J.D. Plummer, Extended defects of ion-implanted GaAs, J. Appl. Phys. 70 (11) (1991) 6790–6795.
[28] S. Leclerc, B. Lacroix, A. Declemy, K. Lorenz, P. Ruterana, Mechanisms of damage formation in Eu-implanted AlN, J. Appl. Phys. 112 (7) (2012) 073525.
[29] B. Lacroix, F. Paumier, R.J. Gaboriaud, Crystal defects and related stress in Y_2O_3 thin films: origin, modeling, and consequence on the stability of the C-type structure, Phys. Rev. B 84 (1) (2011) 014104.
[30] K. Ridier, D. Aureau, B. Berini, Y. Dumont, N. Keller, J. Vigneron, A. Etcheberry, A. Fouchet, Enhanced depth profiling of Perovskite oxide: low defect levels induced in $SrTiO_3$ by argon cluster sputtering, J. Phys. Chem. C 120 (38) (2016) 21358–21363.
[31] S. Takaki, K. Yasuda, T. Yamamoto, S. Matsumura, N. Ishikawa, Atomic structure of ion tracks in Ceria, Nucl. Instrum. Methods Phys. Res. Sect. B-Beam Interact. Mater. Atoms 326 (2014) 140–144.
[32] K. Trachenko, M. Pruneda, E. Artacho, M.T. Dove, Radiation damage effects in the perovskite $CaTiO_3$ and resistance of materials to amorphization, Phys. Rev. B 70 (13) (2004) 134112.
[33] K. Yasuda, C. Kinoshita, S. Matsumura, A.I. Ryazanov, Radiation-induced defect clusters in fully stabilized zirconia irradiated with ions and/or electrons, J. Nucl. Mater. 319 (2003) 74–80.
[34] T.E. Mitchell, L.W. Hobbs, A.H. Heuer, J. Castaing, J. Cadoz, J. Philibert, Interaction between Point defects and dislocations in oxides, Acta Metall. 27 (11) (1979) 1677–1691.
[35] R.W. Whitworth, Charged dislocations in ionic-crystals, Adv. Phys. 24 (2) (1975) 203–304.
[36] A.G. Evans, P.L. Pratt, Dislocations in the fluorite structure, Philos. Mag. 20 (168) (1969) 1213–1237.
[37] K.H.G. Ashbee, F.C. Frank, Dislocations in the fluorite structure, Philos. Mag. 21 (169) (1970) 211–213.
[38] J. Soullard, Evidence for imperfect dislocation loops in irradiated uranium-dioxide samples, J. Nucl. Mater. 78 (1) (1978) 125–130.
[39] B.P. Uberuaga, D.A. Andersson, C.R. Stanek, Defect behavior in oxides: insights from modern atomistic simulation methods, Curr. Opin. Solid State Mater. Sci. 17 (6) (2013) 249–256.
[40] J.M. LeBeau, S. Stemmer, Experimental quantification of annular dark-field images in scanning transmission electron microscopy, Ultramicroscopy 108 (12) (2008) 1653–1658.
[41] M. Herrera, Q.M. Ramasse, D.G. Morgan, D. Gonzalez, J. Pizarro, A. Yáñez, P. Galindo, R. Garcia, M.H. Du, S.B. Zhang, M. Hopkinson, N.D. Browning, Atomic scale high-angle annular dark field STEM analysis of the N configuration in dilute nitrides of GaAs, Phys. Rev. B 80 (12) (2009) 125211.
[42] A. Mostaed, G. Balakrishnan, M.R. Lees, Y. Yasui, L.-J. Chang, R. Beanland, Atomic structure study of the pyrochlore $Yb_2Ti_2O_7$ and its relationship with low-temperature magnetic order, Phys. Rev. B 95 (9) (2017) 094431.
[43] J.J.P. Peters, R. Beanland, M. Alexe, J.W. Cockburn, D.G. Revin, S.Y.Y. Zhang, A.M. Sanchez, Artefacts in geometric phase analysis of compound materials, Ultramicroscopy 157 (2015) 91–97.
[44] J.J.P. Peters, Strain++. http://jjppeters.github.io/Strainpp/.
[45] J. Kioseoglou, G.P. Dimitrakopulos, K. Ph, K. Th, E.C. Aifantis, Dislocation core investigation by geometric phase analysis and the dislocation density tensor, J. Phys. D: Appl. Phys. 41 (3) (2008) 035408.
[46] A. Mostaed, BurgersVectors, 2016. http://wrap.warwick.ac.uk/88297.
[47] G.C. Lau, B.D. Muegge, T.M. McQueen, E.L. Duncan, R.J. Cava, Stuffed rare earth pyrochlore solid solutions, J. Solid State Chem. 179 (10) (2006) 3126–3135.
[48] G. Sala, M.J. Gutmann, D. Prabhakaran, D. Pomaranski, C. Mitchelitis, J.B. Kycia, D.G. Porter, C. Castelnovo, J.P. Goff, Vacancy defects and monopole dynamics in oxygen-deficient pyrochlores, Nat. Mater. 13 (5) (2014) 488–493.
[49] C.R. Stanek, L. Minervini, R.W. Grimes, Nonstoichiometry in $A_2B_2O_7$ pyrochlores, J. Am. Ceram. Soc. 85 (11) (2002) 2792–2798.
[50] F.A. Kröger, H.J. Vink, Solid State Physics—Advances in Research and Applications, Academic Press, New York, 1957.